

Full-Stokes Polarimetry for Visible Light Enabled by an All-Dielectric Metasurface

Yongze Ren, Shihao Guo, Wenqi Zhu, Pengcheng Huo, Sijia Liu, Song Zhang, Peng Chen, Lu Chen, Henri J. Lezec, Amit Agrawal, Yanqing Lu, and Ting Xu*

Decoding arbitrary polarization information from an optical field has triggered unprecedented endeavors in polarization imaging, remote sensing, and information processing. Therefore, developing a polarization detection device with full on-chip integration and miniaturization holds tremendous potential for many areas of optical sciences. Herein, a full-Stokes polarimetry device for visible light based on an all-dielectric metasurface is proposed. By combining both geometric phase and propagation phase modulation, the metasurface to provide two uncorrelated phase profiles for the two orthogonal states of input polarization is designed, which is then used to spatially separate the various polarization states of incident light. Through the use of a millimeter-scale multiplexed metasurface array, successful characterization of the full polarization distribution of space-variant polarization fields is further achieved. This proof-of-concept ultracompact and ultrathin metasurface is expected to open new pathways in full-Stokes polarization detection, machine vision, and navigation.

1. Introduction

Polarization is an intrinsic attribute of light that describes the oscillatory orientation of the electric field along the optical path. However, it is often not captured in a photograph because most image sensors are only sensitive to the intensity and color of the incident field. Separate from spectrally decoding the information about material constituents in an imaging field, such as done using hyperspectral imaging techniques,^[1] polarization metrology can reveal minuscule, and often invisible, characteristics of emitting light sources or scattering objects such as surface stress and roughness. Therefore, polarimetry has found use in a wide range of applications, such as remote sensing,^[2] machine vision,^[3] biomedical imaging,^[4] and surface

analysis.^[5] Traditionally, polarimetry has been realized using either the division-of-time (DoT)^[2–4] or the division-of-aperture (DoA)^[5] technique. In DoT, the intensity of light with different polarization states is recorded by a detector after passing through a rotating wheel equipped with polarizers mounted at different orientation angles. The DoT technique sacrifices temporal resolution, and also requires mechanically moving parts, which is not desirable in an optical setup. In contrast, in DoA, the light is split by a series of polarization optics and recorded by several separate detectors. This approach has the disadvantage of requiring a fairly long propagation space between the various optical components as well as strict alignment between them. In recent years, much of the polarization metrology interest has focused on the development of the division-of-focal plane (DoFP) technique, where a photodetector array is placed at the focal plane covered with different polarization filters.^[6–8] Despite their successful commercialization, DoFP devices are unable to provide a measurement of the full-Stokes parameters, or detection of polarization structured beams with high spatial resolution. Other novel polarimetry approaches, such as using black phosphorus^[9] or graphene,^[10] are still premature and need further development to be integrated into functional devices.


Metasurfaces, consisting of a single layer of subwavelength optical nanoantennas, have provided the ability to arbitrary control multidimensional properties of light, including phase,^[11–15] polarization,^[16–18] frequency,^[19,20] and amplitude.^[21,22] As a result, metasurfaces have been widely explored to tailor the wavefront of incident light for applications in holography,^[23–25]

Y. Ren, S. Guo, P. Huo, S. Liu, S. Zhang, P. Chen, Y. Lu, T. Xu
National Laboratory of Solid-State Microstructures
Jiangsu Key Laboratory of Artificial Functional Materials
College of Engineering and Applied Sciences
Nanjing University
Nanjing 210093, P. R. China
E-mail: xuting@nju.edu.cn

Y. Ren, S. Guo, P. Huo, S. Liu, S. Zhang, P. Chen, Y. Lu, T. Xu
Collaborative Innovation Center of Advanced Microstructures
Nanjing University
Nanjing 210093, P. R. China

W. Zhu, L. Chen, H. J. Lezec, A. Agrawal
Physical Measurement Laboratory
National Institute of Standards and Technology
Gaithersburg, MD 20899, USA

W. Zhu, L. Chen
Maryland NanoCenter
University of Maryland
College Park, MD 20899, USA

 The ORCID identification number(s) for the author(s) of this article can be found under <https://doi.org/10.1002/adpr.202100373>.

© 2022 The Authors. Advanced Photonics Research published by Wiley-VCH GmbH. This is an open access article under the terms of the Creative Commons Attribution License, which permits use, distribution and reproduction in any medium, provided the original work is properly cited.

DOI: 10.1002/adpr.202100373

high-resolution imaging,^[26–28] structural colors,^[29–31] or orbital angular momentum generation.^[32–35] Recently, using diffractive and matrix Fourier optics, a DoA full-Stokes polarization camera has been demonstrated.^[36] Furthermore, using Si metasurfaces, DoFP full-Stokes polarimetry has been demonstrated in the near-infrared spectral range.^[37–40] In addition to dielectric metasurfaces, plasmonic metasurfaces have also been utilized for polarization detection.^[41–45] However, metallic nanostructures suffer from large intrinsic absorption losses, which significantly limit their efficiencies, especially while operating in the transmission mode.

In this work, we propose and experimentally demonstrate DoFP full-Stokes polarimetry for visible light using an all-dielectric metasurface. The metasurface is composed of an array of subwavelength-spaced elliptical-shaped titanium-dioxide (TiO₂) nanopillars acting as nanoscale birefringent waveplates. By combining both geometric phase and propagation phase modulation, we designed the metasurface to provide two uncorrelated phase profiles for the two orthogonal polarization states of the incident light, which is then used to spatially separate the various polarization states of incident light with high efficiency. In addition to detecting arbitrary polarization states of spatially uniform beams, we demonstrate the fabrication of a millimeter-scale metasurface array to successfully map the complete spatially varying polarization distribution of cylindrical vector beam (CVB). Offering the advantages of integration in a compact and ultrathin architecture, we envision this metasurface platform to offer new capabilities for polarization analysis, Stokes holography, and multidimensional imaging.

2. Results and Discussion

Fundamentally, any arbitrary polarization state of a monochromatic plane wave can be represented using the Stokes vector formalism as $\mathbf{S} = [S_0, S_1, S_2, S_3]^T$, where T indicates the transpose of the matrix. The various matrix components are defined as $S_0 = I = I_0 + I_{90} = I_{45} + I_{135} = I_R + I_L$, $S_1 = (I_0 - I_{90})$, $S_2 = (I_{45} - I_{135})$, $S_3 = (I_R - I_L)$, where I is the total incident intensity, I_0 , I_{90} , I_{45} , and I_{135} are the intensities of light with polarization oriented at 0°, 90°, 45°, and 135° with respect to the x -axis, respectively, and I_R (I_L) denotes the intensity of right (left) circularly polarized light (RCP/LCP). Due to the direct quantitative relationship between the polarization states of incident light and intensity of certain polarization basis, the Stokes vector offers enormous simplicity and is therefore widely used in polarization metrology.^[36–46] Here, instead of using a traditional set of optic elements, a single-layer metasurface composed of birefringent TiO₂ nanopillars is designed to split three pairs of orthogonal states of input polarization (0°/90°, 45°/135°, and RCP/LCP) with high efficiency, and simultaneously focus them to different positions on the sensor plane (Figure 1a). The full-Stokes parameters can be obtained by measuring the intensities of the six different polarization bases at the focal plane, and thus the polarization state of incident light can be determined. Figure 1b shows the schematic diagram of the proposed planar metasurface element consisting of three polarization beam splitters spatially arranged in a hexagonal pattern. Each beam splitter occupies a rhomb region and has the ability to separate and focus a pair of

orthogonal polarization states along the diagonal direction. The phase profile of each metasurface beam splitter can be calculated as $\varphi_n = -\frac{2\pi}{\lambda} \left[\sqrt{(x - x_n)^2 + (y - y_n)^2 + f^2} - f \right]$, where x_n and y_n denote the deflecting coordinates of the two polarization states, subscript $n = 1, 2$ represents two orthogonal polarization states, and f is the focal distance of the designed metasurface. Therefore, six different polarization bases (0°/90°, 45°/135°, and RCP/LCP) are equidistantly distributed at the focal plane to form a regular hexagon shape.

For the metasurface to achieve spatial separation of arbitrary orthogonal polarization states ($|k^+\rangle$, $|k^-\rangle$) of the incident light, two independent phase profiles $\varphi_1(x, y)$ and $\varphi_2(x, y)$ should be endowed to the orthogonal input polarization states. In other words, the Jones matrix T of the designed metasurface should simultaneously satisfy the following transformations: $T(x, y)|k^+\rangle = e^{i\varphi_1(x, y)}|k^+\rangle^*$ and $T(x, y)|k^-\rangle = e^{i\varphi_2(x, y)}|k^-\rangle^*$, where $*$ represents complex conjugate. For two orthogonal linear polarizations (e.g., x - and y -polarization, i.e., 0°/90°), the Jones matrix T can be derived as

$$T(x, y) = \begin{bmatrix} e^{i\varphi_1} & 0 \\ 0 & e^{i\varphi_2} \end{bmatrix} \quad (1)$$

According to the diagonal character of matrix T , one can directly obtain the phase shifts $\delta_x = \varphi_1(x, y)$ and $\delta_y = \varphi_2(x, y)$ along the symmetry axes of linearly birefringent nanopillars, which also indicates that for this polarization pair (0°/90°), the metasurface can impart polarization-independent phases by only leveraging the propagation phase offered by the nanostructures with no requirement for nanopillar rotation or geometric phase modulation (Figure 1c). The transmission coefficient and phase shifts along the x -axis are simulated as a function of the in-plane dimensions of TiO₂ nanopillars, and corresponding results are shown in Figure 1d. By discretization of the phase profiles, a series of structural parameters (Table S1, Supporting Information) are selected to provide eight discrete phase levels covering the full 0–2 π phase range and offering high efficiencies at a visible wavelength of 530 nm. In addition, using simple coordinate transformation, the spatial decoupling of 45° and 135° linear polarization states can be realized by rotating every elliptical TiO₂ nanopillar in the previous configuration by 45° relative to the x -axis.

Finally, to spatially decouple the two orthogonal circular polarization states, RCP and LCP, the Jones matrix T can be calculated as^[28]

$$T(x, y) = \frac{1}{2} \begin{bmatrix} e^{i\varphi_1} + e^{i\varphi_2} & -ie^{i\varphi_1} + ie^{i\varphi_2} \\ -ie^{i\varphi_1} + ie^{i\varphi_2} & -e^{i\varphi_1} - e^{-i\varphi_2} \end{bmatrix} \quad (2)$$

The unitary nature and symmetry of this matrix guarantee that it can be diagonalized by solving the characteristic equation. The eigenvalues and eigenvectors of this Jones matrix require that the constituent nanopillars have a birefringent response with phase shifts (φ_x, φ_y) along the two perpendicular symmetry axes, and an orientation angle θ of the fast-axis as a function of the reference coordinate. We can find analytical expressions for required phase shifts and orientation angles as $\varphi_x = (\varphi_1 + \varphi_2)/2$, $\varphi_y = (\varphi_1 - \varphi_2)/2 - \pi$, $\theta = (\varphi_1 - \varphi_2)/4$. In this case, the decoupling

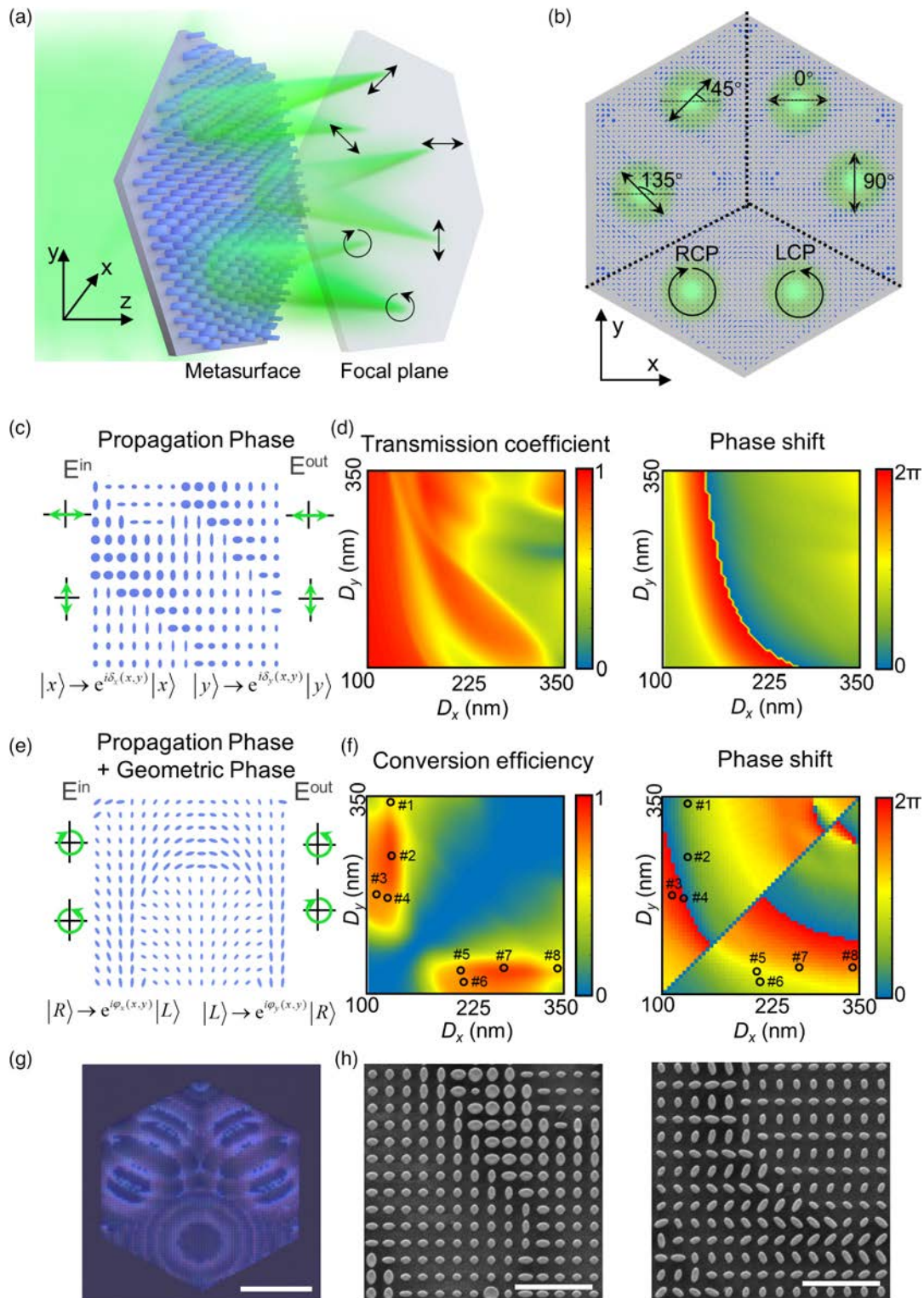


Figure 1. a) Schematic of the designed metasurface consisting of TiO_2 nanopillars on a fused-silica substrate. b) Sketch of the proposed planar metasurface consisting of three polarization beam splitters spatially arranged on a hexagonal pattern. c) Schematic of the $|x\rangle$ and $|y\rangle$ polarization manipulation, which employs only the propagation phase. d) The mapping of transmission coefficient and phase shift along the x -axis as a function of the parameters of slow (D_x) and fast (D_y) axes of the elliptical TiO_2 nanopillars. e) Schematic of the $|L\rangle$ and $|R\rangle$ polarization manipulation achieved by combining propagation and geometric phases. f) The conversion efficiency and phase shift as a function of D_x and D_y . g) Optical photograph of the ortho-hexagonal metasurface. Scale bar: $20\ \mu\text{m}$. h) SEM images of TiO_2 metasurface using only the propagation phase (left) or one that uses both the propagation and the geometrical phases (right). Scale bar: $2\ \mu\text{m}$.

of two orthogonal circular polarization states is achieved through a combination of both the propagation phase and the geometric phase (Figure 1e). Therefore, it is imperative to find a set of nanostructures with varying in-plane dimensions and orientation angles, offering the full $0-2\pi$ phase coverage. Based on the above analysis, eight nanopillar structures with high transmission efficiencies are selected from the calculation results (marked by black circles with #1–#8 in Figure 1f). Figure 1g,h shows an optical photograph and scanning electron microscope (SEM) images of the fabricated TiO_2 metasurface, respectively. The detailed fabrication process is described in the Experimental Section.

Figure 2a shows the custom-built experimental setup for full-Stokes polarization detection. A collimated, linearly polarized input illumination at a free-space wavelength of 530 nm is generated from a supercontinuum laser attached to an acousto-optic tunable filter and a linear polarizer. Subsequently, a half- or a quarter-waveplate (HWP or QWP) is used to tailor the incident light with any discretionary

polarization state before illuminating the metasurface. The transmitted light through the metasurface is then captured using a $50\times$ objective lens and recorded on a charge-coupled device (CCD) camera. To characterize the polarization response of the metasurface device, we first illuminate it with six basis polarization states ($0^\circ/90^\circ$, $45^\circ/135^\circ$, and LCP/RCP) in successive order. The experimental results shown in the first row of Figure 2b demonstrate that the device can route different polarization components to different focal spots. For each incident polarization state, the full intensity distribution at the focal plane is unique, and an obvious extinction can be observed for the focal-spot position corresponding to its orthogonal polarization state. By adding the recorded intensity information at the CCD pixels occupied by each focal spot, the power distribution of the six polarization components can be quantified and the normalized Stokes parameters can be reconstructed (second row of Figure 2b). Figure 2c shows the simulation results of the metasurface device with different input states, including polarization-resolved intensity distribution and the

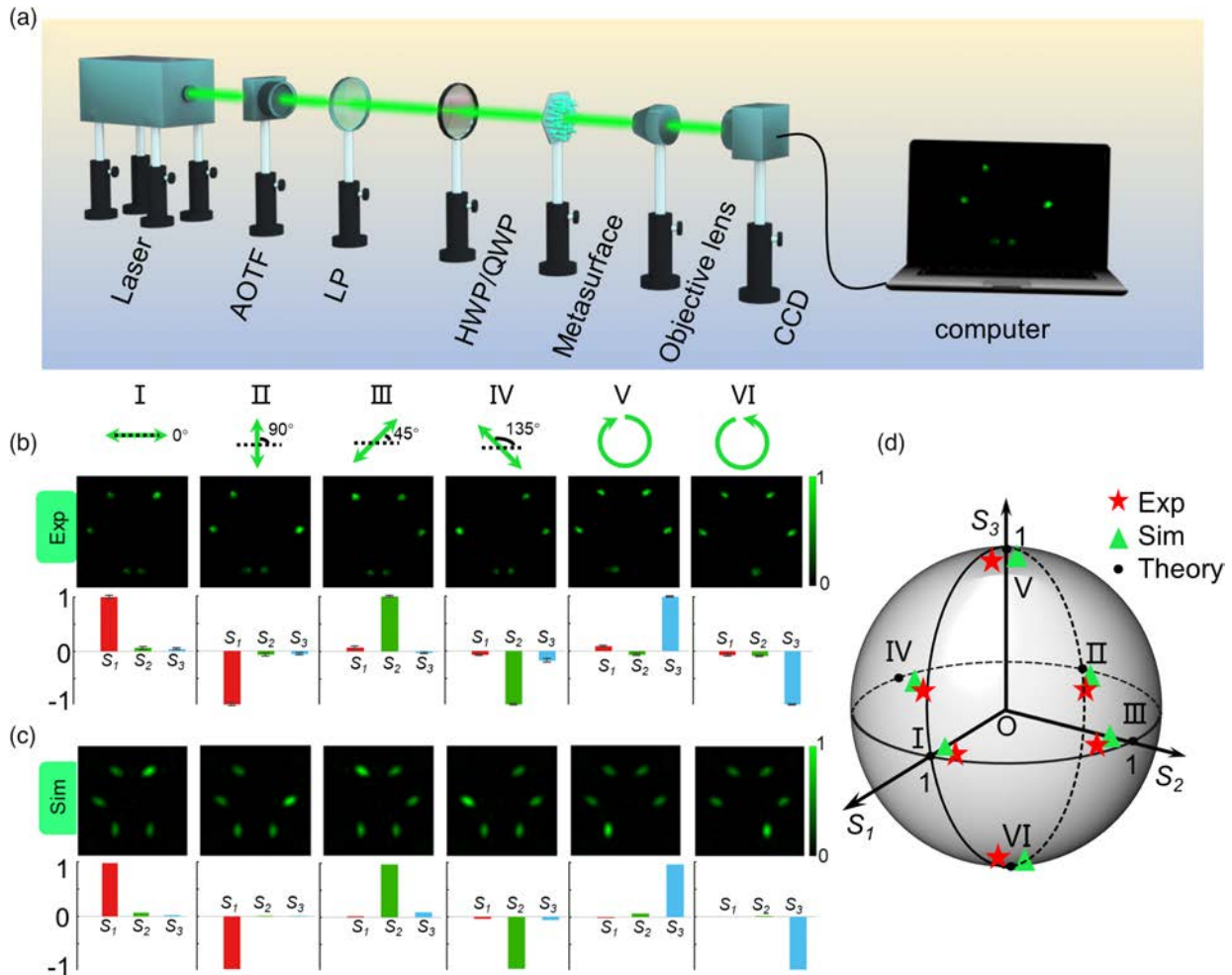


Figure 2. a) Experimental setup for full-Stokes polarimetry. The experimental b) and simulated c) intensity distributions of the metasurface and corresponding reconstructed Stokes parameters for the selected six basis polarization states. The intensity is normalized to the maximum intensity for each polarimetry. Error bars in the experimental results represent standard deviation for repeated measurements. d) The reconstructed Stokes parameters for experimental (red stars), simulated (green triangles), and theoretical (black points) results, plotted on the surface of the Poincaré sphere.

corresponding Stokes parameters. As plotted on the Poincaré sphere (Figure 2d), both the experimentally reconstructed and the numerically simulated Stokes parameters agree well with the theoretical values, and the results of the accuracy analysis using two-norm error are shown in Figure S3a, Supporting Information. Benefiting from reasonable nanostructure design, the transmission efficiency of the metasurface is about 54%. Efficiency can be further improved by leveraging inverse design or an expanded design library that offers higher transmission coefficients while being less susceptible to errors from nanofabrication process variation. The high-quality polarization control capability achieved here ensures that the designed metasurface can be utilized for optical polarimetry.

Next, to validate the detection capability of the device for full-Stokes polarization characterization, eight random polarization

states are selected to illuminate the metasurface. These input polarization states are generated by rotating the HWP and QWP on the basis of linearly polarized light, and can be represented by spherical coordinates (α, β) , where $\alpha/2$ and $\beta/2$ denote the shape and orientation of polarization ellipse (Supporting Information Note 1 for details). As expected, the transmitted beam through the metasurface is separated into six polarization components and focused on different points at the focal plane. **Figure 3a** summarizes the polarization-resolved intensity distributions for each input state and the corresponding normalized Stokes parameters reconstructed from the experimental measurements, which agree well with the results of the numerical simulations (Figure 3b). As shown in Figure 3c, the reconstructed Stokes parameters of experiment and simulation plotted on the Poincaré sphere agree with the theoretical values. The

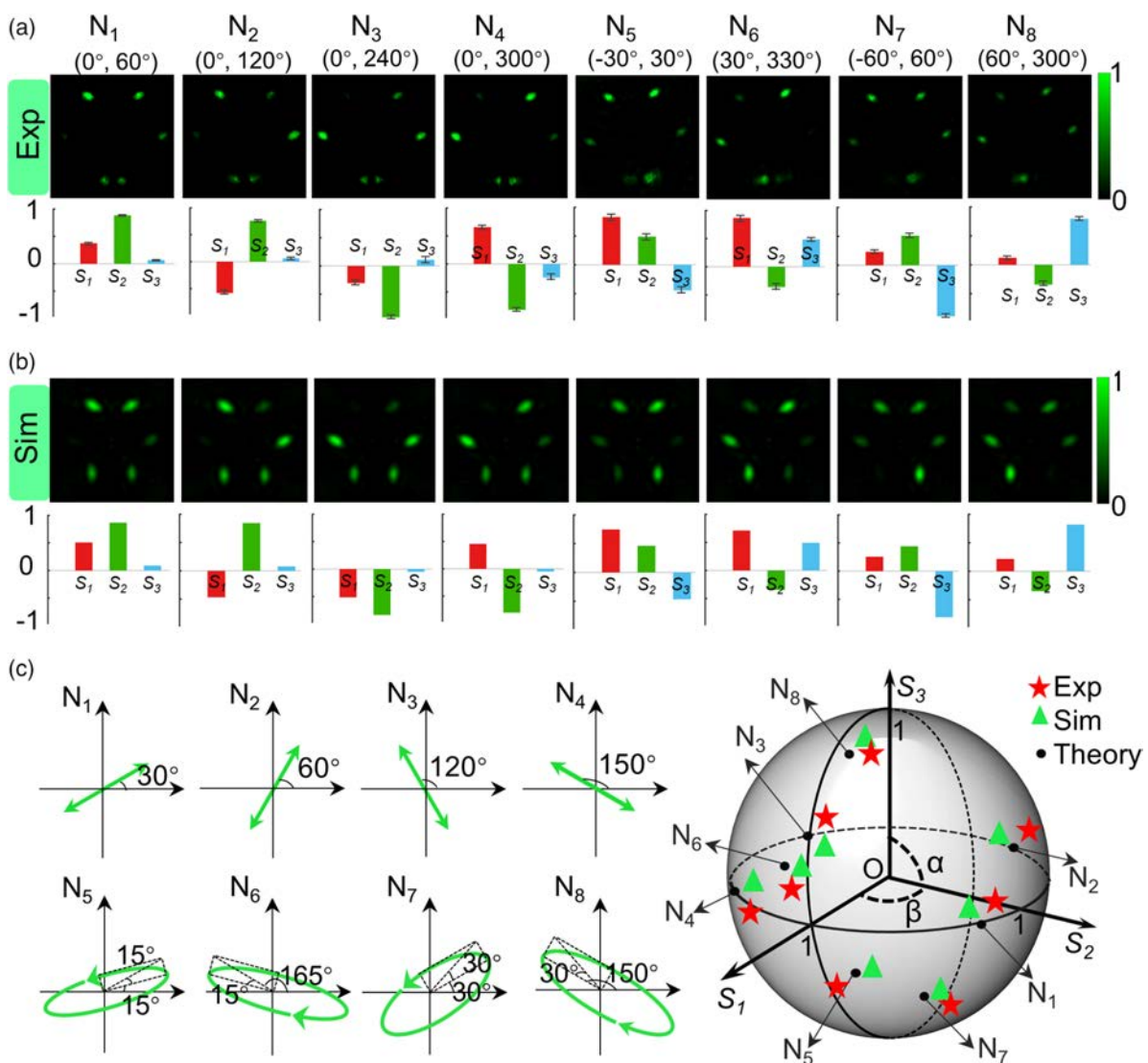


Figure 3. The experimental a) and simulated b) power distributions of the metasurface and corresponding reconstructed Stokes parameters at the selected eight random input polarization states. The intensity is normalized to the maximum intensity for each polarimetry. Error bars in experimental results represent standard deviation for repeated measurements. c) The polarization states of the selected eight input polarizations N_1 – N_8 (left) and corresponding reconstructed Stokes parameters for experimental (red stars), simulated (green triangles), and theoretical (black points) results, plotted on the surface of the Poincaré sphere (right).

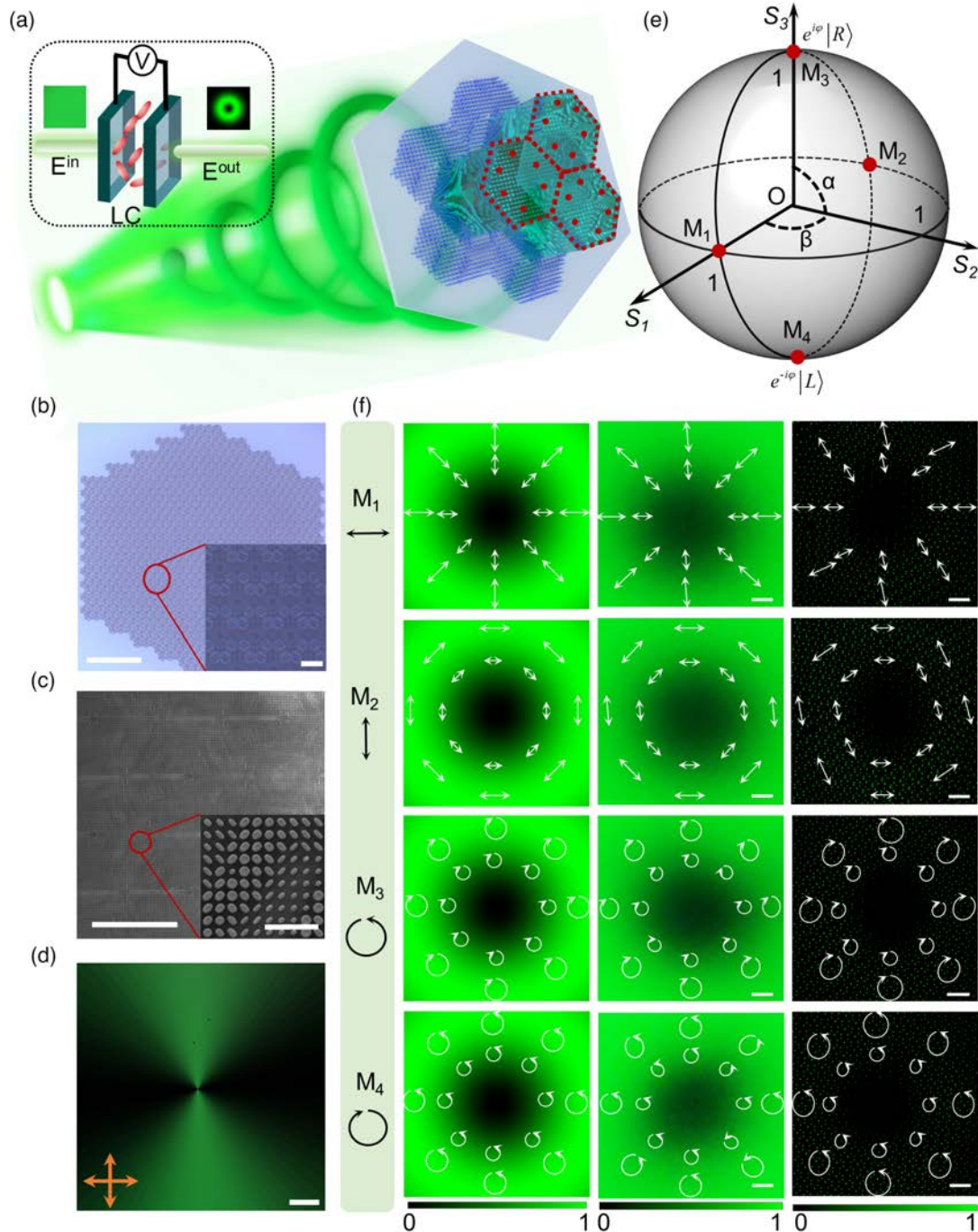


Figure 4. a) Conceptual schematic of the PMA with metasurface pixels arranged on a regular hexagonal pattern. The inset shows the sketch of LC q -plate which when activated with an applied voltage transforms an input plane wave to CVB. b) Optical photograph of the fabricated PMA, scale bar: 250 μm . Bottom inset depicts a magnified optical photograph, scale bar: 20 μm . c) SEM images of the PMA, scale bar: 20 μm . Bottom inset is the magnified SEM, scale bar: 2 μm . d) Optical micrograph of the LC q -plate with $q = +1/2$ measured using a transmittance polarizing microscope (TPM), scale bar: 200 μm . The arrows (bottom) present the orthometric polarizer of TPM. e) The schematic diagram of a HOPS, where the two points on the equator represent the radially (M_1) and azimuthally (M_2) polarized CVB. The two poles (M_3, M_4) have the same ellipticity but opposite topological charges and represented by $e^{i\varphi}|R\rangle$ and $e^{-i\varphi}|L\rangle$, respectively. f) Various CVBs labeled by M_1 – M_4 are generated using the LC q -plate. Left column: Theoretical light field and polarization distribution. Middle column: Experimental light field distributions generated by LC q -plate and polarization distribution detected by traditional DoT polarimetry methods. Scale bar: 50 μm . Right column: Experimental light field distributions with PMA and single-shot reconstructed spatial polarization. Scale bar: 50 μm . The length and direction of the white arrows indicate the intensity and polarization of CVBs, respectively.

accuracy analysis using two-norm error is shown in Figure S3b, Supporting Information.

In addition to identifying a spatially uniform polarized input state, the proposed metasurface device can also be used for the detection of space-variant polarization fields with high spatial resolution. Toward this end, we fabricate a 1 mm diameter polarimetry metasurface array (PMA) composed of sub-metasurface pixels arranged in a hexagonal lattice with a lattice constant of $34\ \mu\text{m}$ (Figure 4a). The optical micrograph of the fabricated PMA and an SEM image of one sub-metasurface pixel are shown in Figure 4b,c, respectively. To demonstrate the versatility and verify the performance of this metasurface platform, we fabricate a liquid crystal (LC) q -plate (Figure 4d) to generate a CVB with space-variant polarization fields. The detailed fabrication process of LC q -plate is described in the Experimental Section. The CVB is generated by superimposing two orthogonal circularly polarized optical vortex beams carrying topological charges of $l = \pm 1$ (Supporting Information Note 2 for details).

The experimental setup used for the detection of space-variant polarization fields is shown in Figure S4, Supporting Information. A square-wave electric function of 5.8 V and 1 kHz is applied to satisfy the half-wave condition of 530 nm and maximize the conversion efficiency. For x - and y -linearly polarized beams incident on such an LC q -plate, a radially and azimuthally polarized CVB is respectively generated and marked by M_1 and M_2 on the higher-order Poincaré sphere (HOPS). M_3 and M_4 are the two poles of HOPS corresponding to the LCP and RCP incident waves, respectively (Figure 4e). As shown in the left column of Figure 4f, for the cross section of each theoretically calculated CVB, the polarization state varies with the coordinate position and results in donut-shaped intensity distribution. Here, the theoretical polarization distributions are calculated and indicated by white arrows whose length and direction denote the strength and polarization state of the incident beam. As a reference, the middle column of Figure 4f shows the experimentally measured intensity patterns of CVB and corresponding reconstructed polarization distributions based on the traditional DoT polarimetry method using bulk optical elements (HWP and QWP), which are used to verify the polarization distribution of the incident beam (Figure S5, Supporting Information). To demonstrate the polarization detection of space-variant polarization fields by the proposed DoFP metasurface device, each CVB is directly projected onto the PMA. An objective lens is used to collect polarization-resolved intensity distribution at the focal plane. Figure 4f (right column) illustrates the experimental results for different CVB input states labeled by M_1 – M_4 . The 13×13 metasurface pixel array can be clearly identified in each image. Here, the direction of each white arrow denotes the polarization information, which is derived from each metasurface pixel by calculating the normalized Stokes parameters. At the same time, the intensity information can be obtained by averaging the power of three rhombus areas within each of the metasurface pixels and are denoted by the length of each white arrow. Compared to traditional polarimetry methods, the proposed PMA does not need bulk optical elements and has the advantage of performing measurement in a single shot. The experimental results achieved here agree well with the theoretical predictions and demonstrate that polarization manipulating metasurface optics can enable

full-Stokes detection and be used as an integrated component in devices or systems requiring in-line polarization metrology.

3. Conclusion

In conclusion, we propose and demonstrate DoFP full-Stokes polarimetry for visible light based on an all-dielectric metasurface platform. By tailoring the propagation and geometrical phases offered by constituent TiO_2 birefringent nanopillars placed on a hexagonal lattice, we designed metasurfaces to split and focus three pairs of orthogonal polarization states of light to six spatially separated focal positions. To validate the metasurface performance, eight random states of input polarization are generated and measured using the metasurface polarimeter, verifying good polarization measurement capabilities of the metasurface. Furthermore, a large-scale metasurface array is fabricated to successfully characterize the full polarization distribution of a CVB generated by an LC q -plate. We envision the lightweight and ultracompact all-dielectric metasurface platform proposed here to provide promising capabilities for integrated polarization metrology and multidimensional imaging.

4. Experimental Section

Metasurface Fabrication: Double-side polished fused-silica substrates were first coated with a layer of hexamethyldisilazane and positive-tone electron beam resist (ZEP520A) with the thickness of 600 nm. Subsequently, samples were coated with 10 nm aluminum via thermal evaporation to avoid charging effects during the electron-beam lithography (EBL) step. The EBL was used to expose the designed pattern at an accelerating voltage of 100 kV. Next, the patterned samples were coated with TiO_2 using the atomic layer deposition (ALD) process at the temperature of 90°C . Later, overcoated TiO_2 layer of ALD was etched by inductively coupled plasma reactive ion etching until the resist was exposed. Finally, the samples were exposed to UV irradiation and soaked by n -methyl-2-pyrrolidone to remove the resist.

LC q -Plate Fabrication: Indium-tin-oxide glass substrates were cleaned and then spin-coated with the UV-polarization-sensitive photoalignment agent dissolved in dimethylformamide at 0.3 wt%. After curing at 100°C , two pieces of substrates were sealed with a $6\ \mu\text{m}$ thick spacer to form a cell. Then, it was placed at the imaging plane of a digital-micro-mirror-based dynamic photo-patterning system^[47,48] to receive the space-variant UV polarization exposure. Afterward, the optical axis distribution of the q -plate was imprinted into the orientations of the photoalignment agent, which would further guide the orientations of LCs. Finally, nematic LC E7 (HCCH, China) was infiltrated into the photo-patterned cell at 80°C and gradually cooled to room temperature, yielding an electrically tunable q -plate.

Supporting Information

Supporting Information is available from the Wiley Online Library or from the author.

Acknowledgements

Y.R. and S.G. contributed equally to this work. This work was supported in part by the National Natural Science Foundation of China (12004175) and the Fundamental Research Funds for the Central Universities. W.Z., L.C., and A.A. acknowledge the support under the Cooperative Research

Agreement between the University of Maryland and the National Institute of Standards and Technology Center for Nanoscale Science and Technology, Award #70NANB14H209.

Conflict of Interest

The authors declare no conflict of interest.

Data Availability Statement

The data that support the findings of this study are available from the corresponding author upon reasonable request.

Keywords

full-Stokes parameters, metasurface, polarimetry, polarization

Received: January 21, 2022

Revised: January 27, 2022

Published online: February 20, 2022

-
- [1] F. Yesilkoy, E. Arvelo, Y. Jahani, M. Liu, A. Tittl, V. Cevher, Y. Kivshar, H. Altug, *Nat. Photonics* **2019**, *13*, 390.
- [2] J. Tyo, D. Goldstein, D. Chenault, J. Shaw, *Appl. Opt.* **2006**, *45*, 5453.
- [3] Y. Zhu, Y. Dong, Y. Yao, L. Si, Y. Liu, H. He, H. Ma, *Biomed. Opt. Express* **2021**, *12*, 4324.
- [4] V. Tuchin, L. Wang, D. Zimnyakov, *Optical Polarization in Biomedical Applications*, Springer, Berlin **2006**.
- [5] J. Pezzaniti, B. David, in *Proc. SPIE*, California, August 2005.
- [6] G. Nordin, J. Meier, P. Deguzman, M. Jones, *J. Opt. Soc. Am. A* **1999**, *16*, 1168.
- [7] J. Guo, D. Brady, *Appl. Opt.* **2000**, *39*, 1486.
- [8] V. Gruev, J. Spiegel, N. Engheta, *IEEE Int. Symp. on Circuits and Systems*, Kos, May, 2006.
- [9] J. Bullock, M. Amani, J. Cho, Y. Chen, G. Ahn, V. Adinolfi, V. Shrestha, Y. Gao, K. Crozier, Y. Chueh, A. Javey, *Nat. Photonics* **2018**, *12*, 601.
- [10] J. Wei, C. Xu, B. Dong, C. Qiu, C. Lee, *Nat. Photonics* **2021**, *15*, 614.
- [11] N. Yu, P. Genevet, M. Kats, F. Aieta, J. Tetienne, F. Capasso, Z. Gaburro, *Science* **2011**, *334*, 333.
- [12] D. Lin, P. Fan, E. Hasman, M. Brongersma, *Science* **2014**, *345*, 298.
- [13] F. Zhang, M. Pu, X. Li, P. Gao, X. Ma, J. Luo, H. Yu, X. Luo, *Adv. Funct. Mater.* **2017**, *27*, 1704295.
- [14] S. Wang, P. Wu, V. Su, Y. Lai, M. Chen, H. Kuo, B. Chen, Y. Chen, T. Huang, J. Wang, R. Lin, C. Kuan, T. Li, Z. Wang, S. Zhu, D. Tsai, *Nat. Nanotechnol.* **2018**, *13*, 227.
- [15] Y. Hu, L. Li, Y. Wang, M. Meng, L. Jin, X. Luo, Y. Chen, X. Li, S. Xiao, H. Wang, Y. Luo, C. Qiu, H. Duan, *Nano Lett.* **2020**, *20*, 994.
- [16] A. Arbabi, Y. Horie, M. Bagheri, A. Faraon, *Nat. Nanotechnol.* **2015**, *10*, 937.
- [17] J. Mueller, N. Rubin, R. Devlin, B. Groever, F. Capasso, *Phys. Rev. Lett.* **2017**, *118*, 113901.
- [18] X. Ma, M. Pu, X. Li, Y. Gao, X. Luo, *Opto-Electron. Adv.* **2019**, *2*, 180023.
- [19] B. Wang, F. Dong, Q. Li, D. Yang, C. Sun, J. Chen, Z. Song, L. Xu, W. Chu, Y. Xiao, Q. Gong, Y. Li, *Nano Lett.* **2016**, *16*, 5235.
- [20] Y. Bao, Y. Yu, H. Xu, C. Guo, J. Li, S. Sun, Z. Zhou, C. Qiu, X. Wang, *Light-Sci. Appl.* **2019**, *8*, 95.
- [21] A. Overvig, S. Shrestha, S. Malek, M. Lu, A. Stein, C. Zheng, N. Yu, *Light-Sci. Appl.* **2019**, *8*, 92.
- [22] M. Liu, W. Zhu, P. Huo, L. Feng, M. Song, C. Zhang, L. Chen, H. Lezec, Y. Lu, A. Agrawal, T. Xu, *Light-Sci. Appl.* **2021**, *10*, 107.
- [23] G. Zheng, H. Mühlenbernd, M. Kenney, G. Li, *Nat. Nanotechnol.* **2015**, *10*, 308.
- [24] X. Li, L. Chen, Y. Li, X. Zhang, M. Pu, Z. Zhao, X. Ma, Y. Wang, M. Hong, X. Luo, *Sci. Adv.* **2016**, *2*, 1601102.
- [25] H. Ren, X. Fang, J. Jang, J. Bürger, J. Rho, S. Maier, *Nat. Nanotechnol.* **2020**, *15*, 948.
- [26] R. Lin, V. Su, S. Wang, M. Chen, T. Chung, Y. Chen, H. Kuo, J. Chen, J. Chen, Y. Huang, J. Wang, C. Chu, P. Wu, T. Li, Z. Wang, S. Zhu, D. Tsai, *Nat. Nanotechnol.* **2019**, *14*, 227.
- [27] P. Huo, C. Zhang, W. Zhu, M. Liu, S. Zhang, S. Zhang, L. Chen, H. Lezec, A. Agrawal, Y. Lu, T. Xu, *Nano Lett.* **2020**, *20*, 2791.
- [28] A. Minovich, A. Klein, N. Janunts, T. Pertsch, D. Neshev, Y. Kivshar, *Phys. Rev. Lett.* **2011**, *107*, 116802.
- [29] B. Yang, W. Liu, Z. Li, H. Cheng, D. Choi, S. Chen, J. Tian, *Nano Lett.* **2019**, *19*, 4221.
- [30] P. Huo, M. Song, W. Zhu, C. Zhang, L. Chen, H. Lezec, Y. Lu, A. Agrawal, T. Xu, *Optica* **2020**, *7*, 1171.
- [31] W. Yang, S. Xiao, Q. Song, Y. Liu, Y. Wu, S. Wang, J. Yu, J. Han, D. Tsai, *Nat. Commun.* **2020**, *11*, 1864.
- [32] H. Ren, X. Li, Q. Zhang, M. Gu, *Science* **2016**, *352*, 805.
- [33] E. Maguid, I. Yulevich, D. Veksler, V. Kleiner, M. Brongersma, E. Hasman, *Science* **2016**, *352*, 1202.
- [34] Y. Shen, X. Wang, Z. Xie, C. Min, X. Fu, Q. Liu, M. Gong, X. Yuan, *Light-Sci. Appl.* **2019**, *8*, 90.
- [35] Y. Guo, S. Zhang, M. Pu, Q. He, J. Jin, M. Xu, Y. Zhang, P. Gao, X. Luo, *Light-Sci. Appl.* **2021**, *10*, 63.
- [36] N. Rubin, G. D'Aversa, P. Chevalier, Z. Shi, W. Chen, F. Capasso, *Science* **2019**, *365*, eaax1839.
- [37] Z. Yang, Z. Wang, Y. Wang, X. Feng, M. Zhao, Z. Wan, L. Zhu, J. Liu, Y. Huang, J. Xia, M. Wegener, *Nat. Commun.* **2018**, *9*, 4607.
- [38] E. Arbabi, S. Kamali, A. Arbabi, A. Faraon, *ACS Photonics* **2018**, *5*, 3132.
- [39] F. Ding, B. Chang, Q. Wei, L. Huang, X. Guan, S. Bozhevolnyi, *Laser Photonics Rev.* **2020**, *14*, 2000116.
- [40] Y. Wang, Z. Wang, X. Feng, M. Zhao, C. Zeng, G. He, Z. Yang, Y. Zheng, J. Xia, *Photon. Res.* **2020**, *8*, 482.
- [41] A. Pors, M. Nielsen, S. Bozhevolnyi, *Optica* **2015**, *2*, 716.
- [42] F. Ding, A. Pors, Y. Chen, V. Zenin, S. Bozhevolnyi, *ACS Photonics* **2017**, *4*, 943.
- [43] P. Wu, J. Chen, C. Yin, Y. Lai, T. Chung, C. Liao, B. Chen, K. Lee, C. Chuang, C. Wang, D. Tsai, *ACS Photonics* **2018**, *5*, 2568.
- [44] J. Bai, C. Wang, X. Chen, A. Basiri, C. Wang, Y. Yao, *Photon. Res.* **2019**, *7*, 1051.
- [45] L. Li, J. Wang, L. Kang, W. Liu, L. Yu, B. Zheng, M. Brongersma, D. Werner, S. Lan, Y. Shi, Y. Xu, X. Wang, *ACS Nano* **2020**, *14*, 16634.
- [46] F. Ding, Y. Chen, S. Bozhevolnyi, *Appl. Sci.* **2018**, *8*, 594.
- [47] P. Chen, B. Wei, W. Hu, Y. Lu, *Adv. Mater.* **2020**, *32*, 1903665.
- [48] C. Xu, P. Chen, Y. Zhang, X. Fan, Y. Lu, W. Hu, *Appl. Phys. Lett.* **2021**, *118*, 151102.